RSC Advances

PAPER

View Article Online
View Journal | View Issue

Cite this: *RSC Adv.*, 2026, **16**, 26623

Enhanced lithium storage in silicon anodes *via* Sn–Ni heterostructures and graphene conductive networks: interface regulation mechanisms

Li Zhen,[a] Xie Jianing,[b] Sun Lin,[a] Zhang Dawei,[a] Chu Fengfei,[a] Shao Sijia*[a] and Wang Xiaomin*[b]

Silicon-based anodes are considered promising candidates for next-generation lithium-ion batteries because of their ultrahigh theoretical capacity. However, their practical application is still hindered by severe volume variation, low electronic conductivity, and unstable interfacial evolution during repeated lithiation/delithiation. In this work, a Sn–Ni@Si heterostructured silicon-based anode with tunable graphene content was constructed through a facile solution-assisted route followed by thermal treatment. Among the investigated samples, the optimized Sn–Ni@Si-2 composite with 25 wt% graphene exhibited the best overall electrochemical performance, delivering an initial coulombic efficiency of 87.81% at 0.1C and maintaining a reversible capacity of 677.09 mAh g^{-1} after 100 cycles at 0.5C. Structural and electrochemical analyses suggest that the improved performance is associated with the synergistic effects of a continuous graphene conductive framework, improved dispersion of active components, and a stabilized interfacial chemical environment involving Si–O–Sn bonding. The optimized composite also shows reduced charge-transfer resistance and enhanced Li^+ diffusion kinetics compared with the graphene-free counterpart. In addition, density functional theory calculations based on a simplified interfacial model indicate that interfacial electronic coupling may contribute to the enhanced charge-transfer behavior observed experimentally. This work provides a feasible strategy for improving the lithium storage performance of silicon-based anodes through synergistic interfacial regulation and conductive-network design.

Received 1st April 2026
Accepted 8th May 2026

DOI: 10.1039/d6ra02735k

rsc.li/rsc-advances

1. Introduction

In recent years, the growing demand for advanced electronic devices and electric vehicles has driven extensive development of rechargeable lithium-ion batteries (LIBs).[1] Owing to their high energy density, long cycle life, low self-discharge rate, and minimal memory effect, LIBs have been widely adopted in portable electronics and electric mobility applications.[2,3] Conventional commercial LIBs typically employ graphite-based anodes, which exhibit a theoretical specific capacity of only 372 mAh g^{-1}.[3] This limitation increasingly fails to satisfy the requirements of modern energy storage systems,[4] underscoring the need for alternative anode materials. Silicon has emerged as a promising candidate due to its high theoretical capacity of 4200 mAh g^{-1}, the highest among all known anode materials for LIBs.[5] In addition to its exceptional capacity, silicon is abundantly available, accounting for 26.4% of the Earth's crust by mass,[5] which further supports its potential for large-scale application in next-generation high-energy-density batteries, further supporting its potential for widespread application.[3,6,7] Unlike carbon-based materials,[3] which possess a layered structure enabling lithium intercalation, silicon stores lithium through an alloying/dealloying mechanism—a process it shares with other metal-based anodes such as Sn and Ge.[8–10] Silicon undergoes volume expansion of up to 300% during lithiation and delithiation,[11] leading to fragmentation, unstable solid electrolyte interfaces (SEIs), and degradation of electrode structure,[12] which reduces cycling stability.[13,14] Currently, the addition of small percentages of silicon (8–10% in most cases) to graphite anodes is limited commercially, but different phases involve different redox reactions, which can cause changes in both the particles and the solid electrolyte interface (SEI), leading to severe capacity degradation.[14–16]

Considerable efforts have been devoted to improving silicon-based anodes through heterostructured or multicomponent design.[17,18] In particular, coupling Si with Sn-containing phases has been demonstrated to alleviate volume variation, provide additional electrochemically active components, and improve structural stability during cycling.[19–23] Meanwhile, conductive carbon matrices such as graphene and graphdiyne can

[a]*Liaoning Key Laboratory of Chemical Additive Synthesis and Separation, Yingkou Institute of Technology, Yingkou, 115014, China. E-mail: 534718570@qq.com*
[b]*Xinjiang Key Laboratory of Novel Functional Materials Chemistry, College of Chemistry and Environmental Science, Kashi University, Kashi, 844000, Xinjiang, PR China. E-mail: ty.com.cn@126.com*

effectively enhance electron transport, maintain particle dispersion, and buffer the mechanical stress induced by repeated lithiation/delithiation.[23–25] These studies indicate that both interfacial engineering and conductive-network construction are beneficial for improving the electrochemical performance of Si-based anodes.[19,25,26] However, the synergistic integration of SnNi interfacial regulation with a graphene conductive framework remains insufficiently explored, especially with respect to the simultaneous optimization of structural integrity, charge-transfer kinetics, and interfacial stability.[19,25,27]

Despite these advances, silicon-based anode materials still face several critical challenges, including substantial volume variation during cycling, low electronic conductivity, unsatisfactory initial coulombic efficiency, and unstable interfacial evolution.[19,28] Structural nanosizing can relieve mechanical stress to a certain extent, while carbon compositing improves conductivity and helps buffer volume changes.[25,28] In addition, the introduction of metallic components with relatively high conductivity is expected to reduce internal resistance and facilitate charge transfer.[27,28] Nevertheless, achieving a stable balance among high capacity, structural robustness, and interfacial stability remains a major challenge for silicon-based anodes, particularly under repeated alloying/dealloying conditions.[19,25]

In this work, a Sn–Ni@Si heterostructured silicon-based anode with tunable graphene content was constructed to address the intrinsic drawbacks of silicon anodes, including severe volume variation, poor conductivity, and unstable interfacial evolution. Different from previously reported single-component coating or simple carbon-composited strategies, the present design combines a Sn–Ni interfacial phase with a graphene conductive framework to simultaneously regulate structural integrity, charge transport, and interfacial stability.[19,25,27] The optimized Sn–Ni@Si-2 composite exhibits an improved initial coulombic efficiency of 87.81% at 0.1C and maintains a reversible capacity of 677.09 mAh g^{-1} after 100 cycles at 0.5C, together with reduced charge-transfer resistance and enhanced Li^+ diffusion kinetics. Combined electrochemical characterization and simplified DFT analysis further suggest that the improved electrochemical performance originates from the synergistic effects of conductive-network construction and interfacial electronic modulation. This work provides a feasible strategy for the rational design of multicomponent silicon-based anodes through synergistic interface and conductivity engineering.

2. Experiment

2.1 Material synthesis

Dissolve an excess of basic nickel carbonate in an appropriate amount of ammonia solution to prepare a saturated solution, and let it stand for 24 hours. Dissolve 0.3 g of $SnCl_4$ in 10 mL of deionized water. Mix 5 mL, 10 mL, 15 mL, and 20 mL of the saturated ammonium nickel carbonate solution with the $SnCl_4$ solution, respectively, to prepare Reagent A. Mix 0.5 g of silicon nanopowder with 10 mL of anhydrous ethanol and sonicate for 30 minutes to prepare Reagent B. Mix Reagent A with Reagent B and sonicate for another 30 minutes. Subsequently, transfer the mixture to a magnetic stirrer at 90 °C for evaporation to remove the solvent, yielding the $Sn_xNi_yO_2$ precursor. The $Sn_xNi_yO_2$ precursor was transferred to a tube furnace and calcined at 600 °C for 3 hours under an argon atmosphere. The resulting composites were named Sn–Ni@Si-5 mL to Sn–Ni@Si-20 mL, corresponding to the amount of nickel carbonate added, respectively.

2.2 Material characterization

The phase and crystalline state of the samples were determined by X-ray diffraction (XRD) at a scan rate of 10 μm min^{-1}. Scanning electron microscopy (SEM) and transmission electron microscopy (TEM/HRTEM) were used to examine the microstructure, particle distribution, and interfacial structure of the materials. The elemental composition and valence states of the Sn–Ni@Si sample surface were analyzed using X-ray photoelectron spectroscopy (XPS).

2.3 Electrochemical tests

The resulting samples were used as active materials and mixed with a conductive agent (Super P) and binders (CMC and SBR) in a mass ratio of 70 : 15 : 15. An appropriate amount of deionized water was added to form a uniform slurry. The slurry was then evenly coated onto a copper foil substrate, vacuum-dried at 80 °C for 12 hours, and die-cut into circular electrode sheets. The electrode sheets were pressed and then dried again under vacuum for later use. The areal density of the active material in the resulting working electrode was controlled at approximately 3.7 mg cm^{-2}. Assemble CR2032 button cells in an Ar-atmosphere glove box, using lithium foil as the counter electrode and reference electrode, Celgard 2400 as the separator, and an electrolyte composition of 1.0 M $LiPF_6$ in EC : DEC = 1 : 1 vol% with 5.0% FEC and 1.0% VC.

Using the LANHE battery testing system, electrochemical performance was evaluated through cyclic testing at a constant current density within the 0.1–1.5 V voltage window, with ambient temperature maintained between 25 and 35 °C. Electrochemical impedance spectroscopy (EIS) was conducted with a CHI660E electrochemical workstation, and cyclic voltammetry (CV) measurements were carried out at a scan rate of 0.1 mV s^{-1}.[29]

2.4 Calculation details

In this study, all first-principles calculations were carried out based on density functional theory (DFT) within the CASTEP module in Materials Studio.[30] The generalized gradient approximation (GGA) in the Perdew–Burke–Ernzerhof (PBE) form was adopted for the exchange–correlation functional, and ultrasoft pseudopotentials were used to model electron–ion interactions. Long-range van der Waals interactions were incorporated using the Tkatchenko and Scheffler (TS) dispersion correction scheme. After convergence tests ensuring energy errors below 1 meV per atom, a plane-wave cutoff energy of 700 eV was selected, and *k*-point sampling was conducted with

a 3 × 3 × 2 Monkhorst–Pack grid. During geometry optimization, all atomic positions were fully relaxed until the following convergence thresholds were reached: self-consistent field (SCF) tolerance below 1×10^{-6} eV per atom, energy change per atom less than 1×10^{-5} eV, maximum atomic displacement below 0.001 Å, and maximum Hellmann–Feynman force below 0.03 eV $Å^{-1}$.[31,32]

3. Results and discussion

3.1 Electrochemical analysis

The electrochemical performance of the samples was evaluated using a half-cell configuration. Cyclic voltammetry (CV) measurements were performed within a potential window of 0.01–1.5 V at a scan rate of 0.1 mV s^{-1} to probe the redox behavior and reversibility of the electrode materials.[33] As shown in Fig. 1a, the initial five CV curves of sample A are presented. In the first cathodic scan, two pronounced reduction peaks located at approximately 0.77 and 0.42 V can be primarily ascribed to electrolyte decomposition and the concomitant formation of the solid electrolyte interphase (SEI) layer. These peaks gradually diminish in subsequent cycles, suggesting reduced irreversible interfacial reactions and the formation of a relatively more stable electrode/electrolyte interface. A distinct cathodic peak emerging at ~0.17 V is associated with the alloying reaction of Si with Li, leading to the formation of amorphous Li_xSi (Si → Li_xSi). During the subsequent anodic process, two oxidation peaks centered at ~0.35 and ~0.51 V are observed, corresponding to the stepwise dealloying of Li_xSi to Si.[34] Notably, the anodic peak intensities progressively increase upon cycling without significant shifts in peak positions, suggesting an activation process and improved electrochemical reversibility. This behavior can be attributed to the gradual stabilization of the electrode/electrolyte interface and enhanced utilization of active materials, implying favorable structural integrity of the Sn–Ni@Si composite during repeated lithiation/delithiation.[35]

The initial galvanostatic charge–discharge profiles of all samples, measured at 0.1C within a voltage window of 0.01–1.5 V, are presented in Fig. 1b.[36] At 0.1C, sample A delivers a high initial discharge capacity of 3247.05 mAh g^{-1} with a coulombic efficiency of 80.22%. In comparison, samples B, C, and D exhibit lower initial discharge capacities of 1942.47, 1612.32, and 1680.12 mAh g^{-1}, accompanied by coulombic efficiencies of 64.79%, 54.52%, and 55.77%, respectively. When the current density is increased to 0.5C, the initial discharge capacity of sample A decreases to 2146.98 mAh g^{-1} while maintaining a coulombic efficiency of 78.08%. Under identical conditions, samples B, C, and D deliver capacities of 1064.04, 684.91, and 731.47 mAh g^{-1}, with improved coulombic efficiencies of 80.68%, 79.90%, and 79.03%, respectively. Research has shown that while increasing the tin–nickel content can improve structural stability and electrical conductivity, it may also reduce the relative proportion of active silicon, thereby creating a trade-off between capacity and cycling stability. An increase in nickel (Ni) content typically leads to a decrease in initial discharge capacity at low current densities. While higher tin–nickel (Sn–Ni) content can improve conductivity and buffering effects, excessive addition may reduce the effective silicon (Si) content, resulting in a decrease in specific capacity.

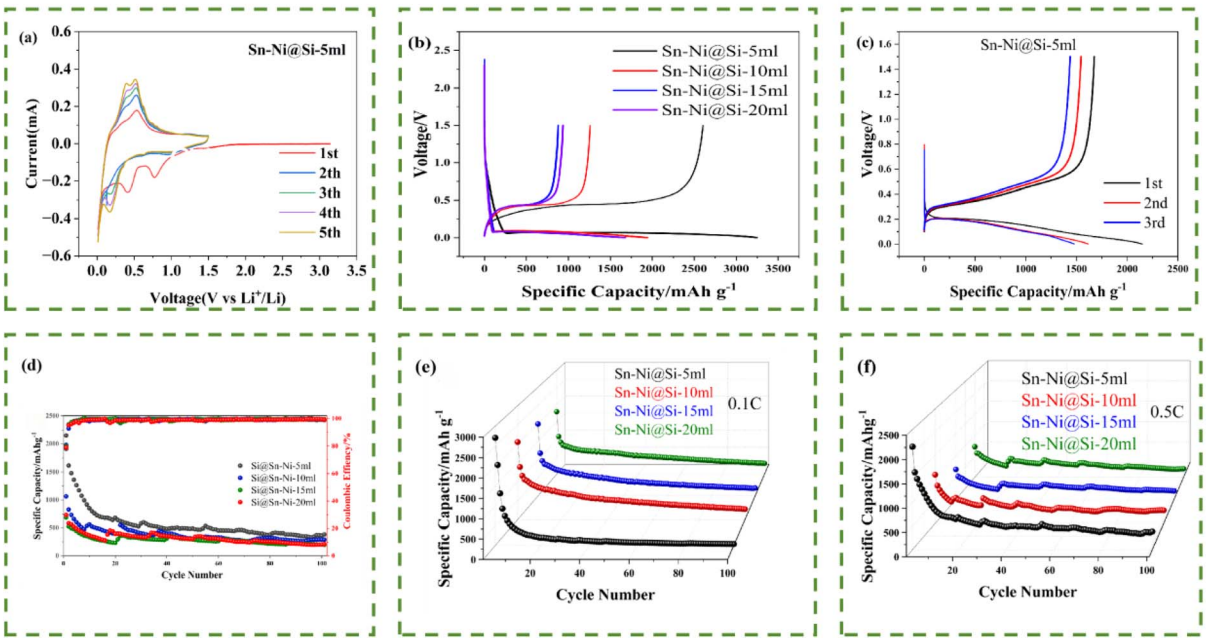

Fig. 1 Electrochemical performance of the Sn–Ni@Si samples without graphene: (a) cyclic voltammetry (CV) curves of sample A measured at 0.1 mV s^{-1}; (b) initial galvanostatic charge/discharge curves of samples A–D at 0.1C; (c) first three galvanostatic charge/discharge profiles of sample A at 0.5C; (d) cycling performance of samples A–D at 0.5C; and (e and f) comparison of the cycling performance of sample A at 0.1C and 0.5C.

Meanwhile, the variation in initial coulombic efficiency becomes less pronounced at higher current density, suggesting similar interfacial reaction behavior under fast charge–discharge conditions.

Fig. 1c shows the galvanostatic charge–discharge profiles of the Sn–Ni@Si composite (sample A) over the first three cycles at 0.5C. The first discharge curve exhibits a long and flat plateau, corresponding to the alloying reaction between Li and Si to form Li–Si phases.[37] The subsequent cycles display highly overlapping profiles, indicating good electrochemical reversibility. Combined with the CV results, this behavior suggests a relatively more stable interfacial evolution during the initial cycles, which may be associated with reduced continuous SEI reconstruction.[38] The cycling performance of the electrodes was evaluated at 0.5C, as shown in Fig. 1d. A general trade-off between initial capacity and cycling stability is observed with increasing Sn/Ni content. Sample A delivers the highest initial capacity of 2146.98 mAh g^{-1} but undergoes rapid capacity decay, retaining only 487.3 mAh g^{-1} after 50 cycles. In contrast, samples with higher Sn/Ni content exhibit lower initial capacities but improved capacity retention. Further cycling tests at 0.1C and 0.5C (Fig. 1e and f) reveal a more gradual capacity decay at lower current density. After 100 cycles, the reversible capacities follow the order: sample D (316.5 mAh g^{-1}) > sample B (277.4 mAh g^{-1}) > sample C (219.4 mAh g^{-1}) > sample A (36 mAh g^{-1}), indicating enhanced cycling stability with increased Sn/Ni incorporation.

The improved cycling stability can be attributed to the synergistic effects of Sn and Ni. The formation of Sn–Ni phases provides an electrically conductive framework and acts as a buffering matrix to mitigate the volume variation of Si during repeated lithiation and delithiation. However, excessive incorporation of Sn/Ni reduces the fraction of active Si, leading to decreased capacity. For sample A, the rapid capacity fading is likely associated with severe volume expansion of Si, resulting in electrode pulverization, unstable solid electrolyte interphase, and loss of electrical contact during cycling.

3.2 Micromorphological characterization

The morphology and elemental distribution of sample A (Sn–Ni@Si-5 mL) were characterized using scanning electron microscopy (SEM), transmission electron microscopy (TEM), and energy-dispersive X-ray spectroscopy (EDS), as shown in Fig. 2. Fig. 2a–f reveal that the composite exhibits an irregular aggregate structure, with particles of varying sizes and shapes, indicating a heterogeneous morphology. Fig. 2g–i present TEM images of the sample, revealing distinct lattice fringes at the interface corresponding to SnO_2, which can be attributed to the SnO_2(110) crystal plane (JCPDS No. 41-1445). The SnO_2 at the interface may help buffer the volume changes of silicon during charge–discharge cycles and maintain local electron transport pathways. Elemental mapping results (Fig. 2j) show that Sn and Ni are distributed relatively uniformly throughout the composite, with some overlapping regions, indicating close

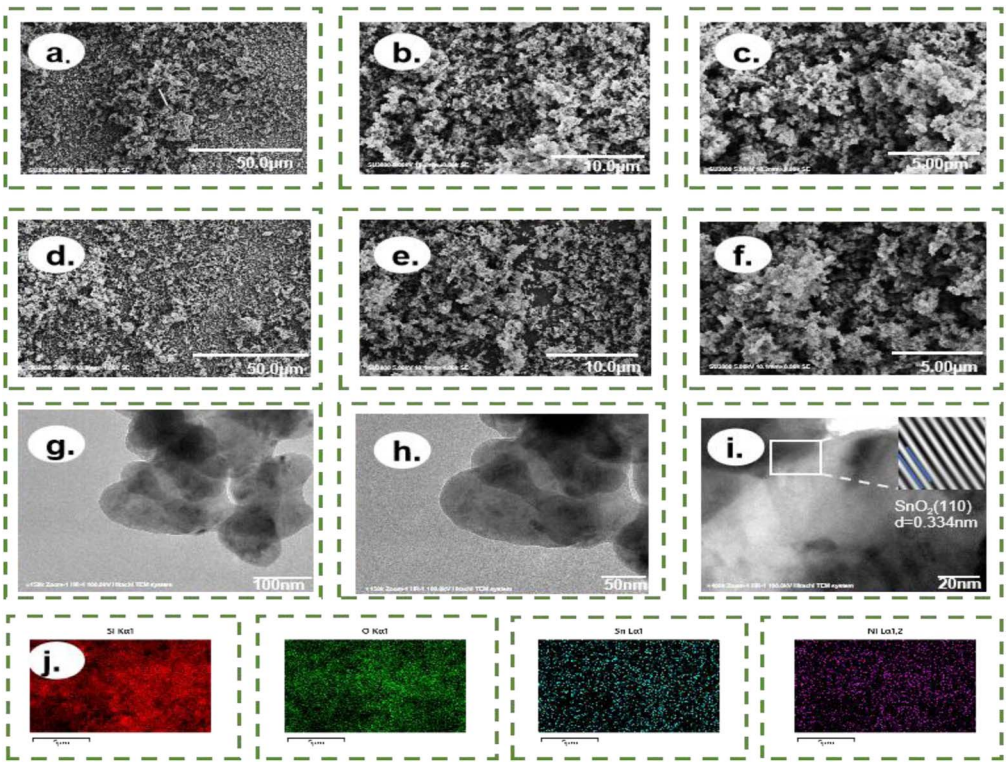

Fig. 2 Morphology and elemental distribution of sample A: (a–f) scanning electron microscope (SEM) images at different magnifications; (g–i) transmission electron microscope (TEM) images; and (j) corresponding energy-dispersive X-ray spectroscopy (EDS) maps of Si, O, Sn, and Ni. A scale bar is included in each image.

contact between these components and the absence of significant phase separation. This distribution facilitates the formation of continuous conductive pathways within the electrode. Furthermore, energy-dispersive X-ray spectroscopy (EDS) analysis indicates the presence of oxygen species on the surface, suggesting partial surface oxidation of the material-a common phenomenon in silicon-based composites exposed to ambient conditions. The silicon detected on the surface is primarily in an oxidized state.

To further elucidate the phase composition and chemical states of the prepared materials, X-ray diffraction (XRD) and X-ray photoelectron spectroscopy (XPS) analyses were subsequently conducted.

Fig. 3a presents the XPS survey spectrum of sample A. The characteristic peaks of Sn are clearly observed, while the Ni-related signal is relatively weak, which is likely due to the low Ni content and the limited surface sensitivity of the XPS measurement. Therefore, the XPS results mainly suggest the participation of Ni-containing species rather than providing a rigorous quantitative determination of Ni content. High-resolution spectra of Si 2p, Sn 3d, and O 1s are shown in Fig. 3b–d. The Si 2p spectrum can be deconvoluted into two components centered at 98.7 and 103.2 eV, corresponding to Si–Si and Si–O bonds, respectively, indicating partial surface oxidation of silicon.[38] The Sn 3d spectrum exhibits two peaks located at 486.6 eV (Sn $3d_{5/2}$) and 495.37 eV (Sn $3d_{3/2}$), arising from spin–orbit splitting. The binding energies are consistent with oxidized Sn species, suggesting the presence of SnO_x on the material surface.[39,40] The O 1s spectrum shows a dominant peak at approximately 532.3 eV, which can be attributed to metal–oxygen bonds (*e.g.*, Sn–O and Si–O), further supporting the existence of surface oxide species.[41]

Fig. 4 presents the XRD pattern of sample A. Distinct diffraction peaks located at $2\theta = 28.4°$, 47.3°, 56.1°, 69.1°, and 76.4° can be indexed to the (111), (220), (311), (400), and (331) planes of crystalline Si (JCPDS No. 77-2108), indicating that the crystalline structure of Si is well maintained after the synthesis process.[38] The relatively weak diffraction intensity of the oxide and intermetallic phases may be attributed to their low concentration and possible partial amorphization, which is commonly observed in nanostructured or composite systems. In addition to the Si phase, several weak diffraction peaks can be assigned to SnO_2 (JCPDS No. 41-1445), SiO_2 (JCPDS No. 85-0865), and Ni_3Sn (JCPDS No. 35-1362) phases,[42] suggesting the

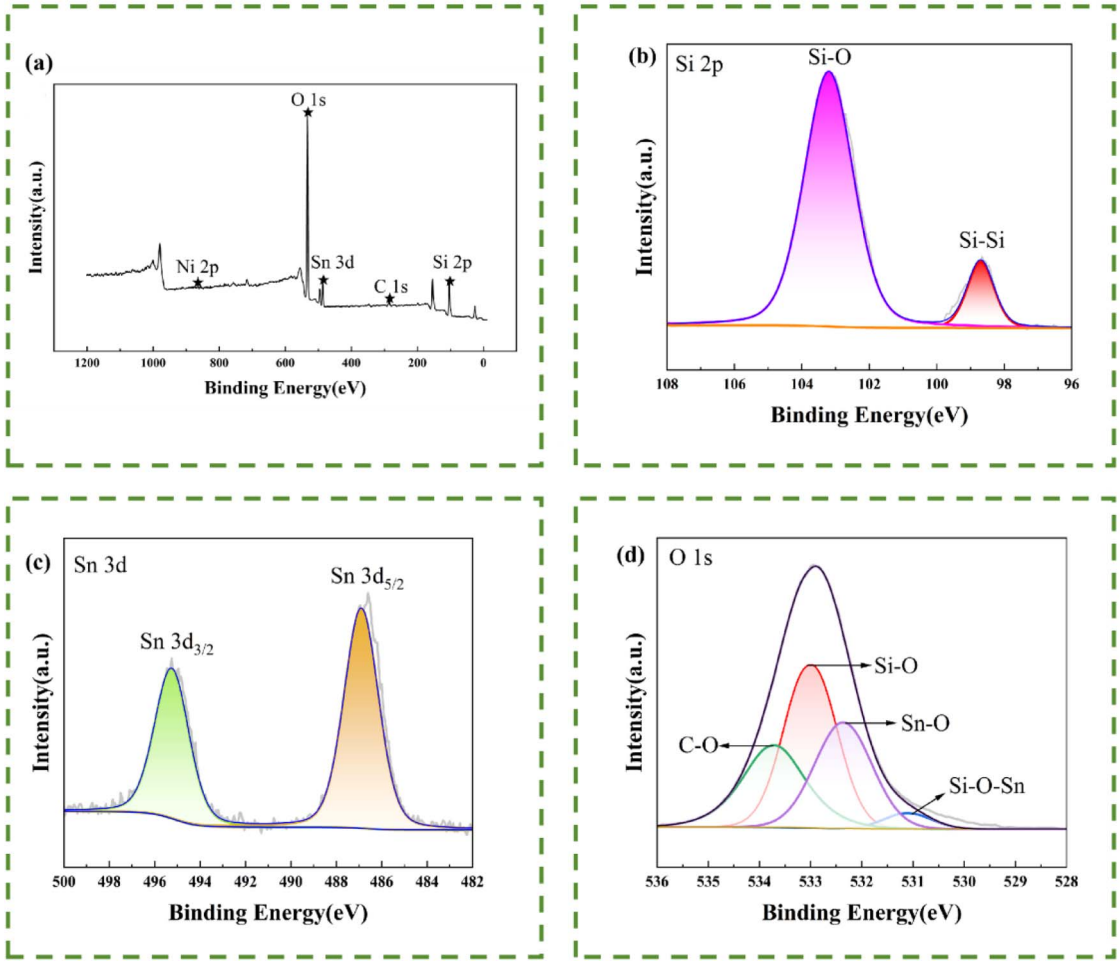

Fig. 3 (a) XPS full-spectrum scan of sample A; (b–d) high-resolution maps of Si/Sn/O elemental.

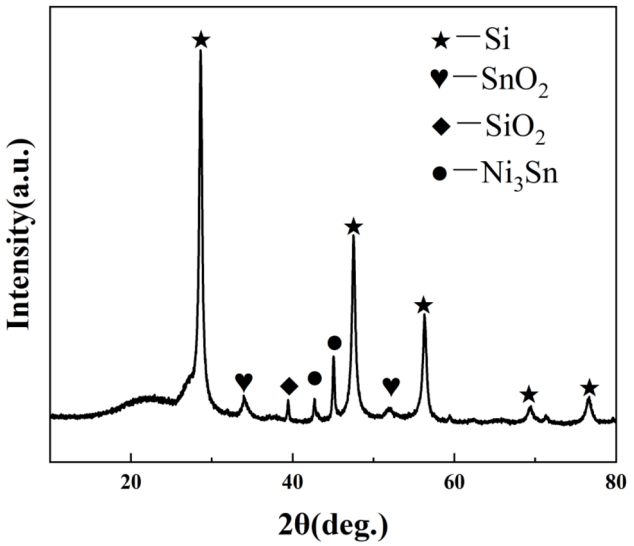

Fig. 4 XRD plot of sample A.

coexistence of oxide species and intermetallic compounds within the composite. The presence of SnO_2 and SiO_2 is consistent with the partial surface oxidation observed in the XPS analysis. The formation of the Ni_3Sn phase is likely attributed to the interaction between Sn and Ni during the synthesis process, which can facilitate the construction of a conductive network and improve structural stability.[43] However, considering the weak intensity of these peaks, the XRD results mainly provide supportive rather than definitive evidence for the presence of Ni-related phases.

Overall, the XRD results confirm the coexistence of crystalline Si, oxide species, and Sn–Ni intermetallic phases, providing structural support for the enhanced electrochemical performance of the composite.

3.3 Characterization of microscopic morphology after addition of graphene

To investigate the effect of graphene incorporation on the structural properties of the composite, different amounts of graphene were introduced into sample A, yielding Sn–Ni@Si-1 (20 wt%), Sn–Ni@Si-2 (25 wt%), and Sn–Ni@Si-3 (30 wt%). The synthesis procedure remained consistent with that described previously. The resulting materials were systematically characterized and evaluated.

The SEM images after graphene incorporation are shown in Fig. 5a–h. For Sn–Ni@Si-1, graphene appears as loosely distributed flakes with incomplete surface coverage, and slight agglomeration of Si, Sn, and Ni particles can still be observed, indicating insufficient structural integration at low graphene content. Correspondingly, the carbon signal in EDS mapping is relatively weak. High-resolution TEM (HRTEM) images of the graphene-containing Sn–Ni@Si sample (Fig. 5i–l) reveal clear lattice fringes corresponding to $Ni_3Sn(101)$ (d = 0.312 nm) (JCPDS No. 35-1362) and Si(111) (d = 0.313 nm) (JCPDS No. 77-2108), indicating well-defined crystalline domains at the interface. The graphene sheets are observed surrounding the composite particles, forming a continuous conductive network that can facilitate electron transport. These observations suggest that the graphene framework helps maintain close contact between Sn–Ni and Si phases, potentially buffering volume changes and supporting interfacial stability during repeated lithiation/delithiation cycles. While this provides direct evidence of local interface integrity, it should be noted that the complete heterostructure including the graphene network is inferred rather than fully quantified.

In contrast, Sn–Ni@Si-2 exhibits a more continuous and interconnected graphene network, within which Si and metal particles are uniformly embedded. The elemental mapping reveals a more homogeneous distribution of C, Sn, Ni, and Si, suggesting improved structural integration. Such a configuration is expected to facilitate the formation of an effective conductive network and enhance electron transport. For Sn–Ni@Si-3, excessive graphene leads to the formation of stacked lamellar structures, as observed in the SEM images. This overcoverage may partially block active sites and hinder ion transport, which could negatively affect electrochemical performance.[44–47]

Energy-dispersive X-ray spectroscopy (EDS) of the graphene-containing Sn–Ni@Si sample indicates a composition of Si 72.7 wt%, O 13.1 wt%, C 10.3 wt%, Sn 2 wt%, and Ni 2 wt% (Fig. 5m and n). The carbon content reflects the presence of graphene, forming a conductive network around the composite particles. Sn and Ni are relatively uniformly distributed with some overlapping regions, suggesting close contact between these components and potential formation of continuous conductive pathways. The presence of oxygen indicates partial surface oxidation of the silicon-based material. These results, combined with TEM observations of lattice fringes at the interface, support the formation of a multicomponent composite with well-integrated Sn–Ni and Si domains embedded in the graphene conductive framework, which may contribute to buffering volume changes and improving interfacial stability during cycling. In addition, the reduced intensity of the O signal compared to the carbon-free sample suggests that graphene may suppress surface oxidation to some extent. The uniformly distributed Si signal also implies improved dispersion of active materials within the carbon matrix.[48,49]

Overall, an appropriate graphene content (25 wt%) not only constructs a continuous conductive network, but also improves the spatial dispersion of Si and Sn–Ni species and strengthens their interfacial contact. Such structural integration is expected to alleviate local stress concentration during repeated lithiation/delithiation, thereby suppressing particle pulverization and maintaining electronic percolation within the electrode. In addition, the reduced surface O signal, the increased fraction of reduced Si species, and the detection of Si–O–Sn bonding collectively suggest that graphene incorporation helps stabilize the local chemical environment and promotes the formation of a more robust interfacial structure. By contrast, insufficient graphene coverage cannot effectively integrate the active components, whereas excessive graphene stacking may partially block active sites and impede ion transport. Therefore, the 25 wt% graphene content provides the most favorable

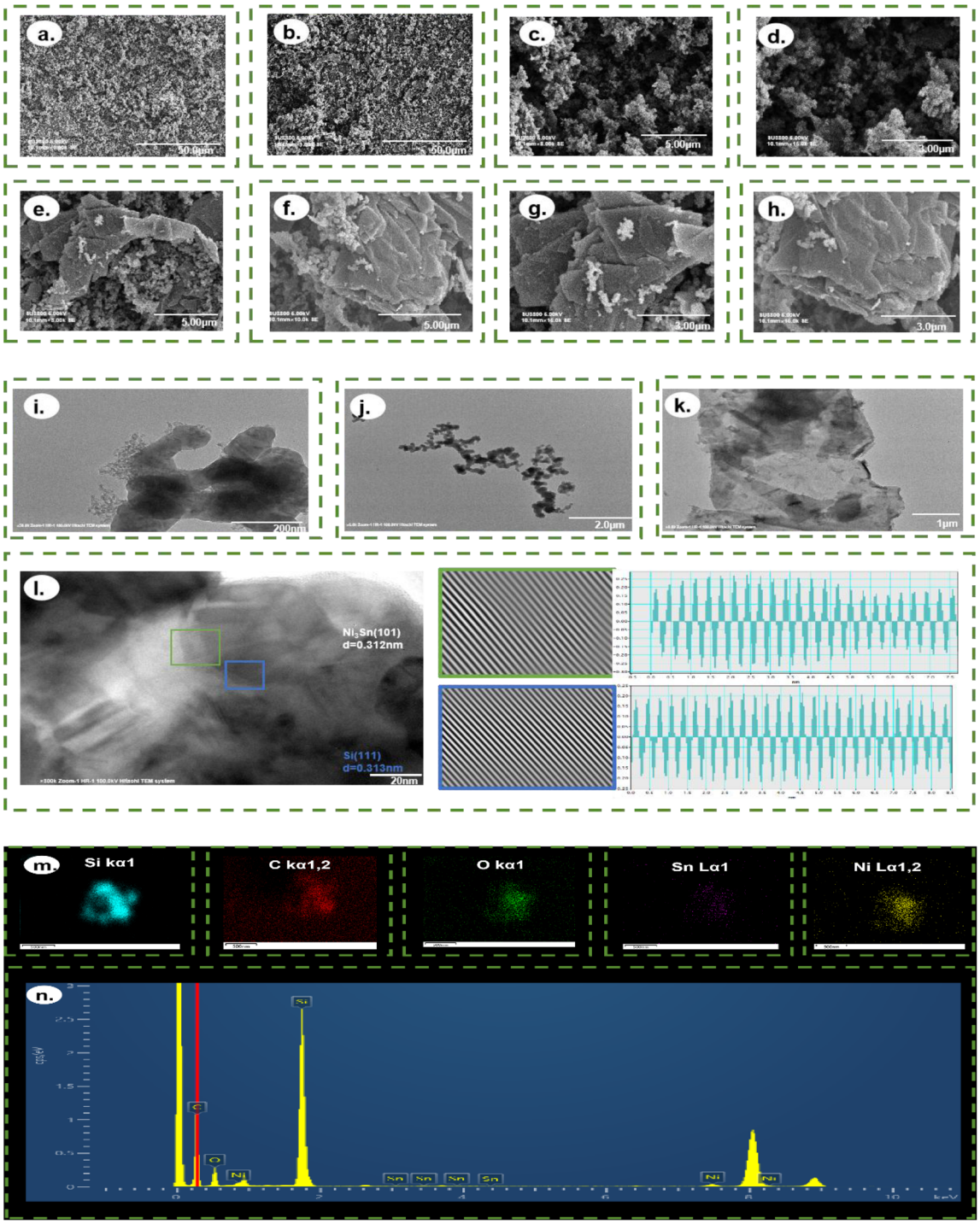

Fig. 5 Morphological and elemental distribution characterization of graphene-containing samples: (a–h) SEM images of the Sn–Ni@Si-1, Sn–Ni@Si-2, and Sn–Ni@Si-3 samples at different magnifications; (i–l) TEM images; and corresponding EDS elemental distribution maps for Si, C, O, Sn, and Ni (m and n). A scale bar is provided in each image.

balance among structural integrity, interfacial stability, and electron/ion transport.

Fig. 6a presents the XRD patterns of the samples with different graphene contents. Compared with the graphene-free sample, the diffraction peaks associated with Sn-containing phases become less pronounced with increasing graphene content, which may be attributed to the reduced crystallinity or lower detectable content of these phases after graphene incorporation.

To further investigate the chemical states and interfacial characteristics, XPS analysis was performed. As shown in the high-resolution spectra, Sn is present in both metallic and

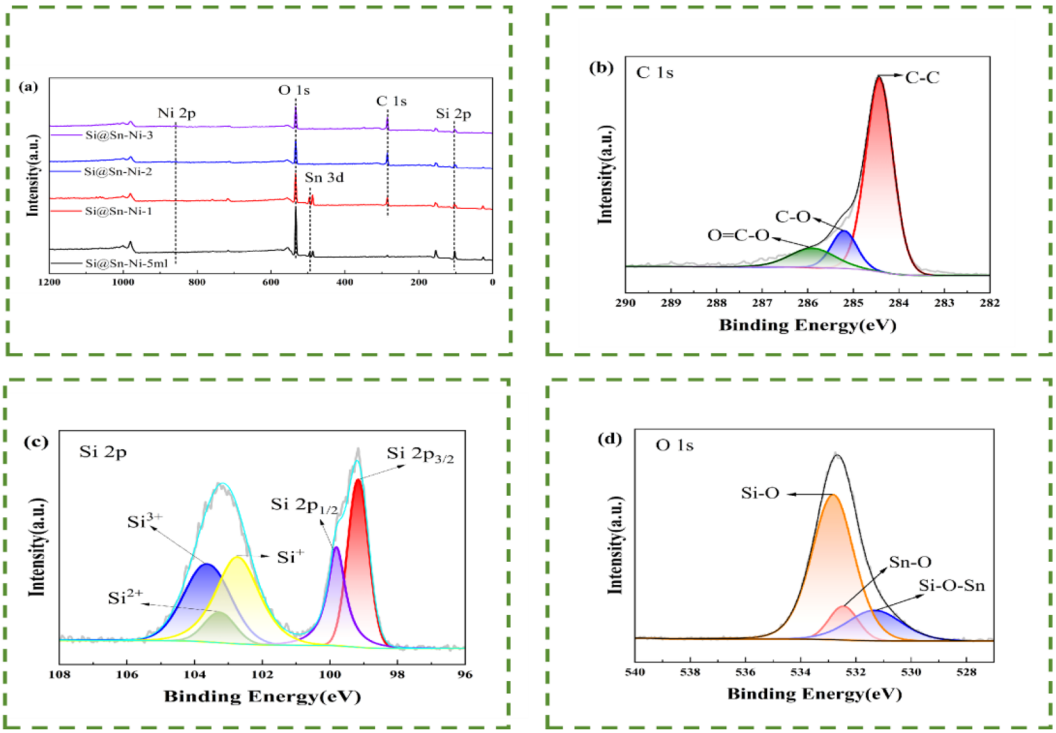

Fig. 6 XPS characterization of the graphene-containing samples: (a) survey spectra of all samples; (b) high-resolution C 1s spectrum of Sn–Ni@Si-2; (c) high-resolution Si 2p spectrum; and (d) high-resolution O 1s spectrum.

oxidized states, indicating the coexistence of multiple Sn species. The O 1s spectrum exhibits peaks at approximately 532.6 and 531.5 eV, which can be assigned to metal–oxygen bonds (*e.g.*, Sn–O) and interfacial bonding configurations such as Si–O–Sn, respectively.[50,51] These results suggest the presence of interfacial interactions between Si, Sn, and oxygen-containing species.

Taking sample 2 as a representative example, the deconvoluted C 1s spectrum (Fig. 6b) shows three main components at 284.4, 285.2, and 285.9 eV, corresponding to C–C, C–O, and O=C–O bonds, respectively. The dominant C–C peak indicates that graphene largely retains its sp^2 carbon structure, while the presence of oxygen-containing functional groups suggests partial surface oxidation of carbon species.[38]

As shown in Fig. 6c and d, the Si 2p spectrum exhibits a slight shift toward lower binding energy after graphene incorporation, indicating an increased proportion of reduced Si species. Quantitative analysis reveals that the fraction of Si^0 increases from 55% to 78%, while a certain proportion of interfacial Si–O–Sn species is also detected. This behavior suggests that graphene may play a role in stabilizing the reduced state of Si and modifying the interfacial chemical environment.[52–55]

Fig. 7 presents the X-ray diffraction (XRD) patterns of all samples. Prominent diffraction peaks located at $2\theta = 28.4°$, 47.3°, 56.1°, 69.1°, and 76.4° can be indexed to the (111), (220), (311), (400), and (331) planes of crystalline Si,[56] respectively, indicating that the incorporation of graphene does not alter the crystalline structure of Si (JCPDS No. 77-2108). For sample group 1, additional diffraction peaks at $2\theta = 30.7°$ and 32.1° corresponding to SnO_2 (JCPDS No. 86-2264) are observed, which may arise from localized exposure of the active components, possibly associated with non-uniform carbon coverage. Meanwhile, the significant attenuation of SiO_2-related peaks suggests a suppressed oxidation of Si in the presence of graphene.

In sample group 2, a noticeable decrease in the intensity of the Si (111) peak, along with a slight shift of the (220) peak, is observed. Such variations may be indicative of lattice distortion and interfacial interactions between Si and the surrounding matrix. These features are consistent with the presence of a conductive graphene framework that could modulate the local structural environment and promote interfacial coupling among Si, Sn, and Ni. However, further characterization is required to unambiguously verify the formation of heterojunctions.[57,58]

3.4 Electrochemical analysis after adding graphene

The electrochemical performance of the as-prepared samples was evaluated in half-cells using cyclic voltammetry (CV) and galvanostatic charge–discharge measurements. As shown in Fig. 8a–c, all samples exhibit three cathodic peaks during the first cycle. The initial two peaks are associated with the formation of the solid electrolyte interphase (SEI), while the characteristic peak at ~0.17 V corresponds to the alloying reaction of Si with Li to form amorphous Li_xSi. The subsequent anodic peaks located at ~0.26–0.30 V and ~0.54 V are attributed to the dealloying process.

Among all samples, Sn–Ni@Si-2 shows the smallest SEI-related peak area, suggesting that graphene incorporation

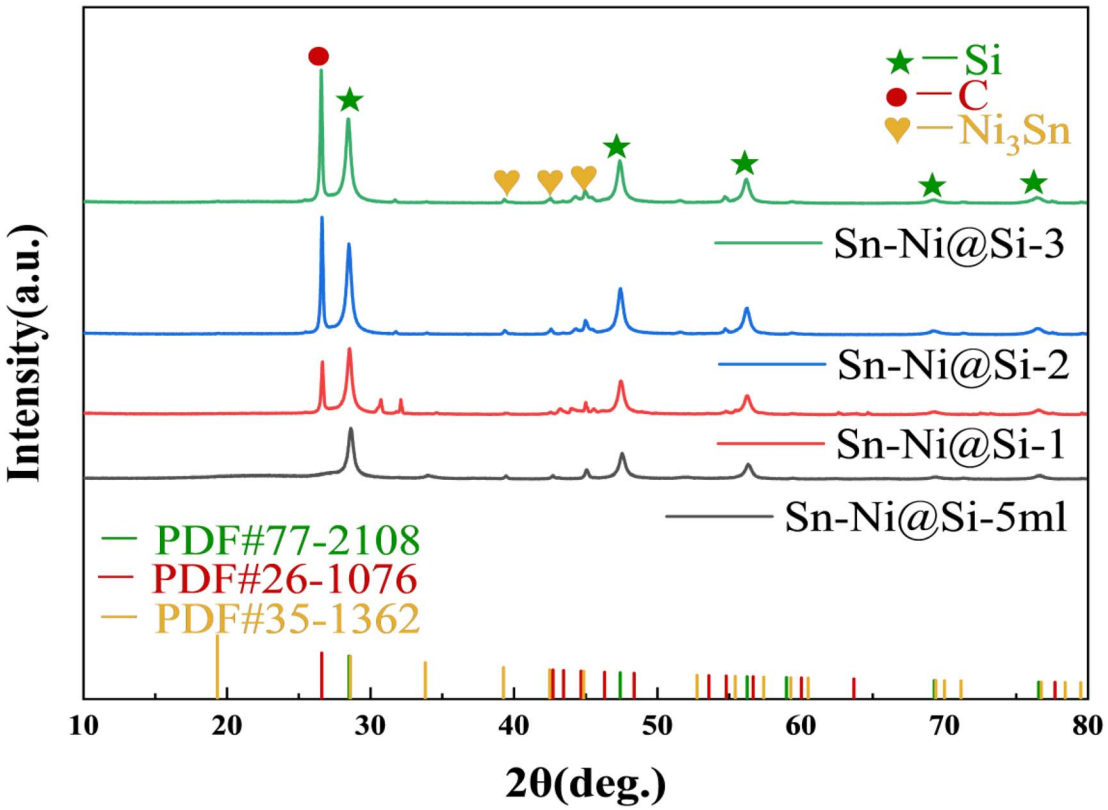

Fig. 7 X-ray diffraction (XRD) patterns of all investigated samples, showing the phase evolution after graphene incorporation.

effectively suppresses irreversible interfacial reactions during the initial lithiation process. Moreover, the CV curves from the 2nd to 3rd cycles exhibit an overlap exceeding 90%, indicating highly reversible electrochemical behavior and a more stable electrode/electrolyte interface. This result implies that the optimized graphene content not only improves electrical contact within the electrode, but also contributes to a more stable interfacial evolution during early cycling.

The initial charge–discharge curves (Fig. 8d and Table 1) show that the discharge capacity gradually decreases with increasing graphene content, while the initial coulombic efficiency (ICE) of each sample remains relatively stable. At a 0.1C rate, Sn–Ni@Si-2 exhibits moderate discharge capacity and relatively high ICE, indicating an optimal balance between active material utilization and interfacial stability.

At higher rates (0.5C), all samples exhibit reduced capacities. Nevertheless, Sn–Ni@Si-2 retains ~74.2% of its low-rate capacity, outperforming Sn–Ni@Si-3, where excessive graphene stacking likely hinders Li^+ diffusion, and Sn–Ni@Si-1, where incomplete graphene coverage limits the effective utilization of active material. This result indicates that the electrochemical role of graphene is not simply dependent on its amount, but rather on how effectively it constructs an interconnected conductive framework around the active particles. With an optimized content, graphene can preserve charge-transport pathways even under repeated volume variation, thereby improving rate capability and reducing polarization.

As shown in Fig. 8e, after three cycles, Sn–Ni@Si-2 exhibited a reversible capacity of 1388.7 mAh g^{-1} at a 0.5C rate, equivalent to 61.98% of its capacity at a 0.1C rate, with a capacity decay of only 6.97%. This is consistent with the high overlap of the CV curves, confirming its excellent cycling stability.

Electrochemical impedance spectroscopy (EIS) was further conducted to investigate charge-transfer and ion-diffusion kinetics. As shown in Fig. 8f and g, all samples display a typical Nyquist profile consisting of a high-frequency semicircle and a low-frequency Warburg tail, corresponding to charge-transfer resistance (R_{ct}) and Li^+ diffusion, respectively.[59] Notably, Sn–Ni@Si-2 exhibits the lowest R_{ct} value (73.04 Ω), which is significantly reduced compared with the graphene-free counterpart, indicating that the introduction of graphene markedly accelerates interfacial charge transfer. The Li^+ diffusion coefficient derived from the Warburg slope (Fig. 8h) further confirms that Sn–Ni@Si-2 possesses the most favorable ion-transport properties ($D \approx 1.71 \times 10^{-13}$ cm^2 s^{-1}). Combined with the structural characterization results, these findings suggest that the optimized graphene framework enhances electron transport, while the Si–O–Sn interfacial structure and improved particle dispersion help maintain open ion-transport channels during cycling. As a result, both charge-transfer kinetics and Li^+ diffusion are simultaneously improved.

$$D = \frac{R^2T^2}{2A^2n^4F^4C^2\sigma^2} \quad (1)$$

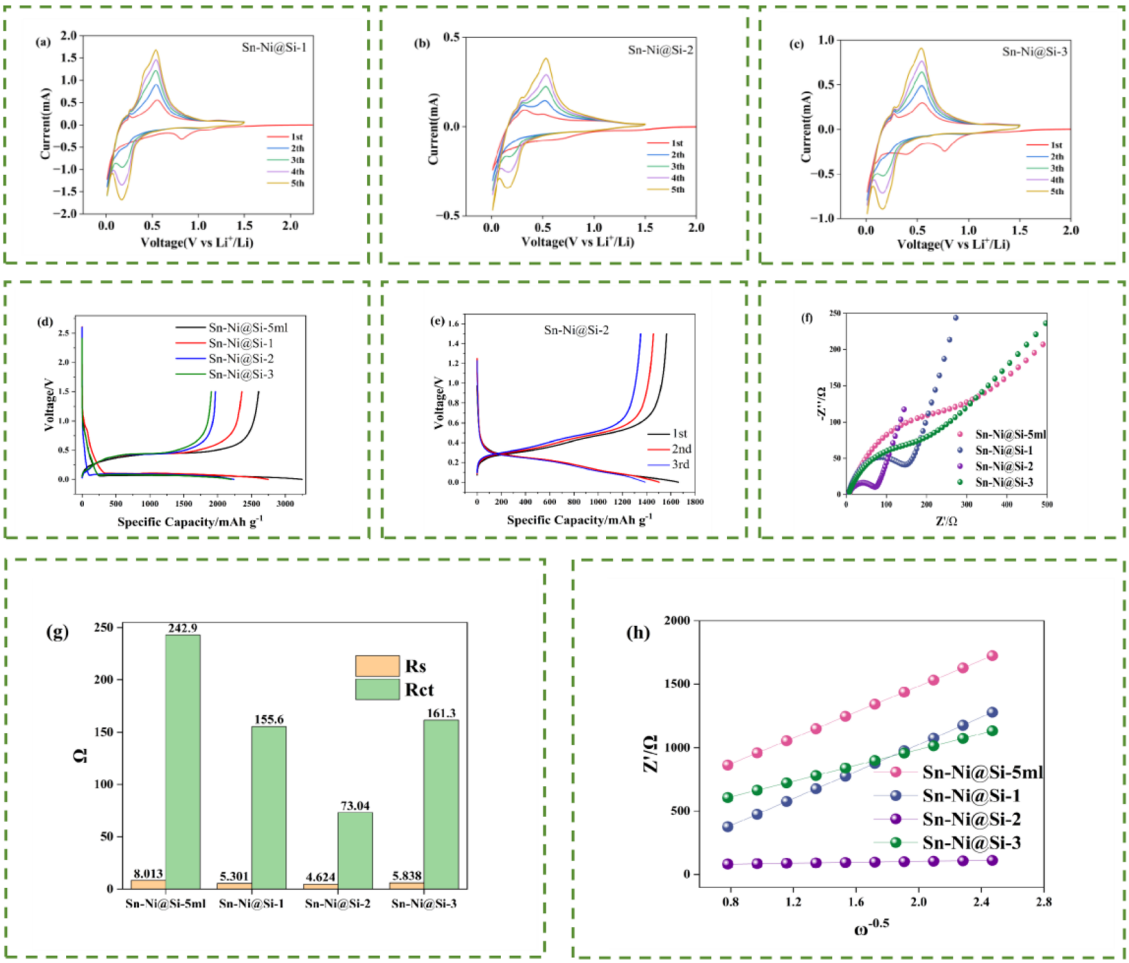

Fig. 8 Electrochemical performance of the graphene-containing samples: (a–c) cyclic voltammetry (CV) curves of the investigated samples measured in the voltage range of 0.01–1.5 V at a scan rate of 0.1 mV s^{-1}; (d) initial galvanostatic charge/discharge profiles recorded at 0.1C; (e) first three galvanostatic charge/discharge profiles of Sn–Ni@Si-2 at 0.5C; (f) electrochemical impedance spectroscopy (EIS) Nyquist plots of the samples; (g) fitted solution resistance (R_s) and charge-transfer resistance (R_{ct}) values; and (h) linear relationship between Z' and $\omega^{-1/2}$ used to evaluate Li^+ diffusion behavior.

Table 1 First discharge capacity and ICE of samples at 0.1C and 0.5C

Sample	0.1C ICE	First discharge capacity (mAh g^{-1})	0.5C ICE	First discharge capacity (mAh g^{-1})
Sn–Ni@Si-5mL	80.22%	3247.05	78.08%	2146.98
Sn–Ni@Si-1	85.85%	2745.54	95.09%	2060.26
Sn–Ni@Si-2	87.81%	2240.40	94.11%	1663.01
Sn–Ni@Si-3	86.74%	2200.73	96.01%	1560.66

In eqn (1), R denotes the ideal gas constant, T represents the thermodynamic temperature during lithium-ion battery operation, A indicates the electrode area, n is the charge transferred during the redox reaction, F is Faraday's constant, and C is the molar concentration of lithium ions in the active material.[41]

In comparison with sample A, the graphene-incorporated samples exhibit significantly improved long-term cycling stability at 0.5C. As shown in Fig. 9a, the initial discharge capacities of samples 1, 2, and 3 are 2060.26, 1663.01, and 1560.66 mAh g^{-1}, respectively. All samples undergo rapid capacity decay during the initial cycles, which can be attributed to continuous SEI formation and irreversible reactions among SiO_x, Sn, and Li during repeated lithiation/delithiation processes. Notably, all electrodes maintain a high coulombic efficiency exceeding 97% after the initial activation stage. This interpretation is consistent with previous studies showing that conductive carbon frameworks and interfacial engineering can help mitigate interfacial instability in alloying-type anodes.[19]

After 50 cycles, samples 1, 2, and 3 retain capacities of 692.16, 1020.67, and 489.56 mAh g^{-1}, corresponding to capacity

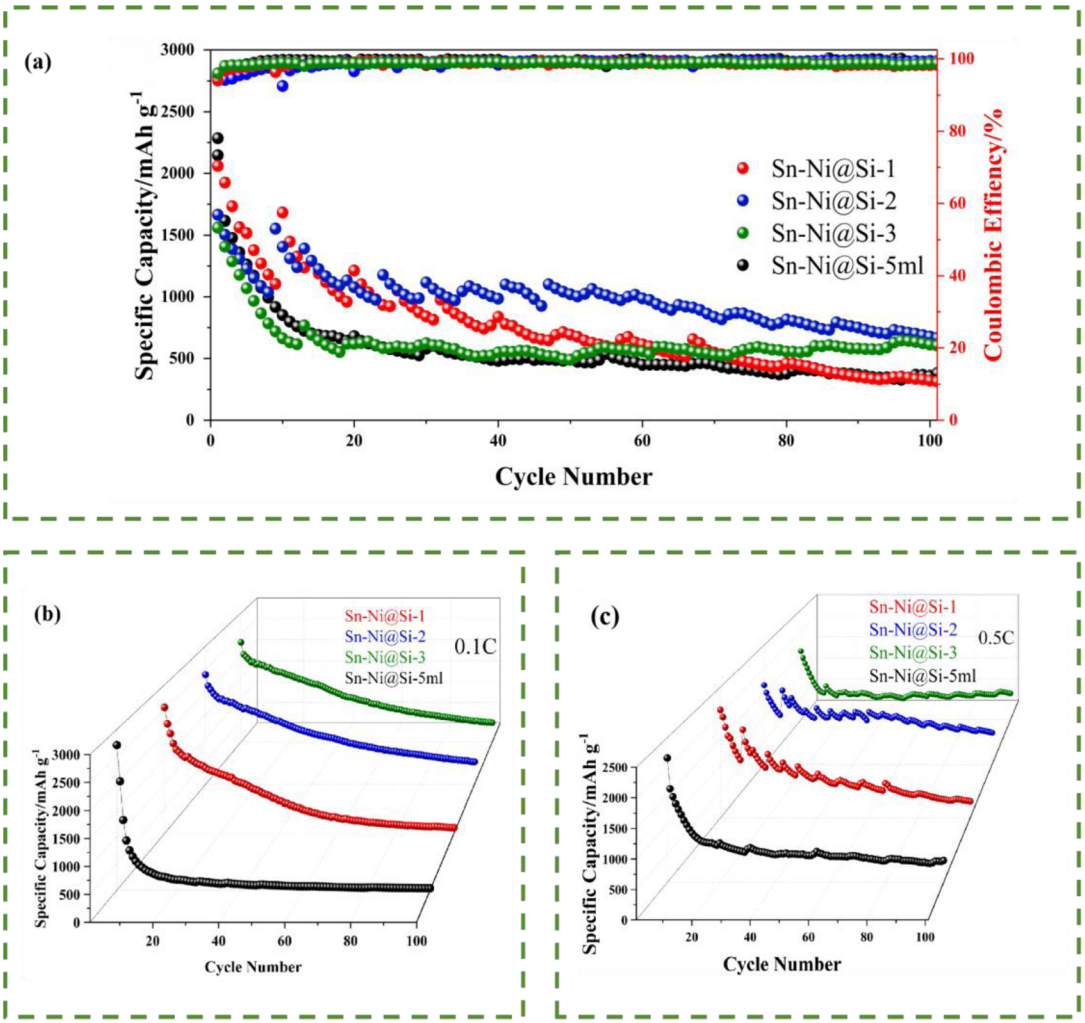

Fig. 9 Cycling performance of the graphene-containing samples over 100 cycles: (a) cycling stability at 0.5C; and (b and c) comparison of the cycling performance at 0.1C and 0.5C.

retention rates of 35.01%, 64.54%, and 32.42%, respectively. After 100 cycles, the capacities further decrease to 321.57, 677.09, and 603.55 mAh g^{-1}, indicating that sample 2 exhibits the most stable cycling performance among all samples. Although the graphene-containing samples exhibit improved cycling stability within 100 cycles, longer-term cycling evaluation is still required to further assess their durability under extended operating conditions. The capacity fading can be attributed to the repeated volume variation of silicon, which leads to particle pulverization, loss of electrical contact, and continuous reconstruction of the electrode/electrolyte interface. In addition, the presence of inactive buffering phases may reduce the overall active material fraction, which also contributes to the observed capacity decay.

Similarly, under long-term cycling at 0.1C (Fig. 9b and c), the graphene-modified electrodes demonstrate markedly enhanced

Table 2 Electrochemical performance comparison of representative Si-based composite anodes reported in the literature and the present work

Sample	Current density/mA g^{-1}	Cycles	Capacity/mAh g^{-1}	ICE	Ref.
SiVC	1000	100	796	62.5%	64
SMG@C	100	75	1124	56.9%	65
Si@WO_3@C	1000	100	610	81%	66
Si–Ni_3Sn_2	300	50	576.6	76%	67
TiO_2/SiO_x/Si	1000	100	421	55%	68
Sn–Ni@Si	500	100	677.09	87.8%	This work
Sn–Ni@Si	100	100	493.5	80.5%	This work

stability compared with sample A, which retains only 36 mAh g^{-1} after 100 cycles. In contrast, samples 1, 2, and 3 deliver capacities of 116.3, 493.5, and 451.8 mAh g^{-1}, respectively. The superior cycling stability of the graphene-containing samples can be attributed to the multiple functions of graphene in the composite electrode. First, graphene forms a continuous conductive framework that improves electronic transport and helps preserve electrical contact among active particles during repeated cycling. Second, the flexible carbon network can partially buffer the volume variation of Si, thereby alleviate stress accumulation and suppress particle pulverization. Third, graphene incorporation promotes the formation of a Si–O–Sn interfacial phase and a more stable local chemical environment, which together help stabilize the electrode/electrolyte interface and mitigate irreversible side reactions. Therefore, the optimized Sn–Ni@Si-2 sample achieves the best balance between mechanical integrity, conductivity, and interfacial stability, resulting in the most stable long-term cycling performance among all investigated samples.

Interestingly, the cycling curves of the graphene-containing samples exhibit slight fluctuations (sawtooth-like features) accompanied by partial capacity recovery during prolonged cycling. This behavior is commonly associated with gradual electrode activation, where previously inaccessible active sites become electrochemically available due to structural rearrangement, electrolyte penetration, and the dynamic evolution of the SEI layer. Such activation processes have been widely reported in Si-based and transition metal oxide anodes. At the initial stage, the presence of Sn and Ni may partially limit the accessibility of Si to Li^+, while continuous cycling facilitates electrolyte infiltration into the interior of the electrode through microstructural evolution (*e.g.*, cracks and pores), thereby progressively activating additional Si domains. This gradual activation contributes to the observed capacity recovery behavior.[60–63]

This study also systematically compared the electrochemical performance of various silicon-based heterostructures and carbon-coated anode materials previously reported. As shown in Table 2, the Sn–Ni@Si composite developed in this study demonstrated relatively good performance in terms of initial coulombic efficiency and cycling stability.

3.5 First principles calculations

To gain insight into the interfacial electronic properties, density functional theory (DFT) calculations were performed on a simplified SnO_2/SiO_x interfacial model.[69–72] It should be noted that this model does not explicitly include Ni or graphene and therefore provides only a partial representation of the experimental Sn–Ni@Si/graphene system. The calculated electronic structure indicates enhanced local charge distribution at the SnO_2/SiO_x interface, which qualitatively supports the experimental observations of improved charge-transfer kinetics and interfacial stability. In combination with TEM observations showing lattice fringes of SnO_2 and EDS mapping confirming close contact of Sn and Ni with Si, these results suggest that the interfacial phases may contribute to buffering volume changes and maintaining electronic pathways during lithiation/delithiation cycles. Therefore, the DFT analysis provides mechanistic insight that complements the experimental characterization without overextending the model beyond its simplifications.

As shown in Fig. 10,[41] both SnO_2 and SiO_x exhibit semiconducting characteristics. The calculated band structures indicate that the Fermi level is located near the valence band maximum (VBM) for both materials. For SnO_2, the conduction band minimum (CBM) and VBM are located at the Γ-point, whereas for SiO_x they are distributed near the X-point.[41,59,63] The calculated band gaps are 1.23 eV for SnO_2 and 0.65 eV for SiO_x.[64] These values are smaller than experimental results, which can

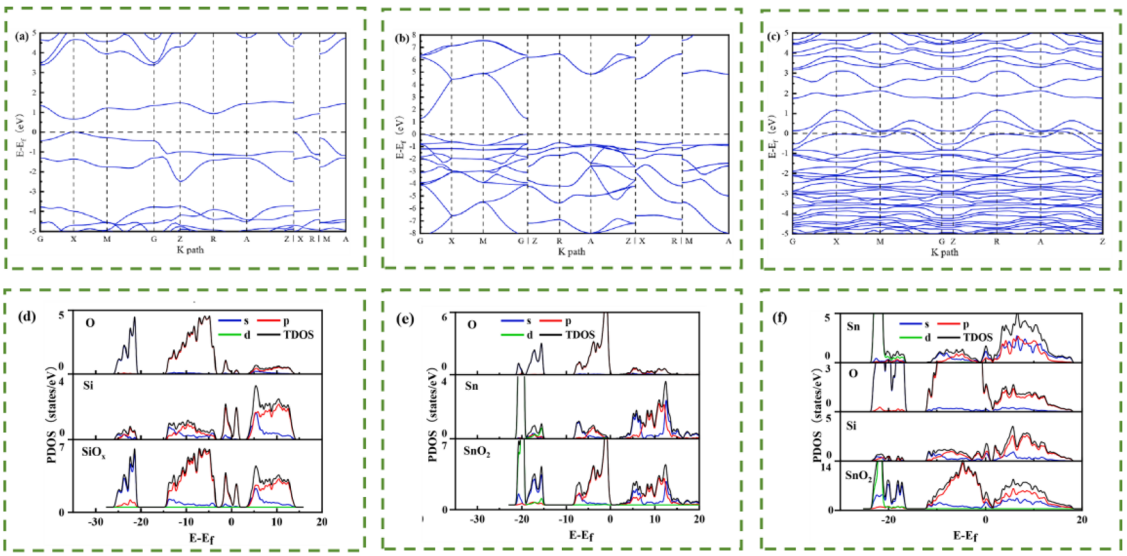

Fig. 10 Electronic energy band structure maps and partial wave state density maps (PDOS) of each sample (a) SiO_x (b) SnO_2 (c) SiO_x@Sn.

be attributed to the well-known bandgap underestimation inherent in standard DFT calculations (*e.g.*, GGA/PBE functionals). Nevertheless, the relative trends in electronic structure remain reliable for qualitative analysis.[65–67]

The total and partial density of states (DOS/PDOS) analyses reveal that, in SiO_x, both the VBM and CBM are primarily dominated by Si 2p and O 2p orbitals, with Si 2p states contributing significantly near the CBM. In SnO_2, the VBM mainly originates from O 2p orbitals with minor contributions from Sn 4d states, while the CBM is dominated by Sn 5s states with hybridization from O 2p orbitals.

Upon formation of the SiO_x@SnO_2 heterostructure, a noticeable shift of the Fermi level toward the valence band is observed, accompanied by an increased density of states near the Fermi level. This indicates enhanced electronic conductivity and suggests strong interfacial electronic coupling between SiO_x and SnO_2.

Furthermore, the PDOS of Sn atoms exhibits a pronounced feature around −1.1 eV below the Fermi level, which can be attributed to the redistribution of electronic states induced by interfacial bonding. This behavior suggests strong chemical interactions at the SiO_x/SnO_2 interface, which facilitate charge transfer and contribute to the formation of a well-coupled heterointerface.[41] These results provide qualitative insight into interfacial electronic behavior and support experimental trends, but do not directly validate the full Sn–Ni@Si/graphene system.

4. Conclusions

In summary, a Sn–Ni@Si multicomponent silicon-based anode with tunable graphene content was successfully prepared, and the influence of graphene incorporation on structure and electrochemical performance was systematically investigated. The results show that an optimized graphene content of 25 wt% is beneficial for constructing a continuous conductive network, improving particle dispersion, and promoting the formation of a Si–O–Sn interfacial environment. As a result, the Sn–Ni@Si-2 composite delivers an improved initial coulombic efficiency of 87.81% at 0.1C and maintains a reversible capacity of 677.09 mAh g^{-1} after 100 cycles at 0.5C. The enhanced electrochemical performance is mainly associated with the synergistic effects of the conductive graphene framework, the buffering role of the Sn–Ni phase, and the interfacial stabilization related to Si–O–Sn bonding. In addition, simplified DFT calculations suggest that local interfacial electronic coupling may contribute to the improved charge-transfer behavior observed experimentally. Although the optimized samples exhibited improved cycling stability over 100 cycles, capacity decay was still observed during long-term cycling; therefore, further long-term cycling tests are required to comprehensively evaluate their durability and practical applicability. Through the synergistic engineering of interfaces and conductivity, this study demonstrates the feasibility of this silicon–tin–nickel modification and provides valuable insights for the rational design of multi-component silicon-based anodes.

Author contributions

Li Zhen and Xie Jianing: conceptualization, methodology, validation, data analysis, writing. Sun Lin: data processing and interpretation, manuscript structuring, writing. Zhang Dawei: mechanical measurement, interpretation. Chu Fengfei: mechanical measurement, interpretation. Shao Sijia: supervision, data analysis, writing-reviewing & editing. Wang Xiaomin: supervision, conceived the idea, data analysis, interpretation, manuscript preparation.

Conflicts of interest

The authors declare that they have no known competing financial interests or personal relationships that could have appeared to influence the work reported in this paper.

Data availability

The authors confirm that the data supporting the findings of this study are available within the article. Additionally, the data cited in this study are publicly available in Elsevier at DOI: https://doi.org/10.1016/j.electacta.2025.145688, with reference number [*Electrochimica Acta*, 145688.]

Acknowledgements

This work was supported by the following grants: the Foundation of Liaoning Key Laboratory of Chemical Additive Synthesis and Separation Project (ZJNK2417). Yingkou joint project of provincial natural science foundation (2024LNYKJ02). Enterprise Doctoral Double Innovation Plan (YKSCJH2024-028). Liaoning Provincial Department of Education Project (LJ212414435010). "Tianchi Talent" Introduction Program.

References

1 H. lin Ren, J. jie Wang, Y. Su, S. Zhao, wei Li Cheng, X. min Wang and Bo han Li, WO_3 coating improves the cyclic stability of $LiNi_{0.9}Co_{0.05}Mn_{0.05}$ as cathode materials for lithium-ion batteries, *Electrochim. Acta*, 2024, **503**, 144913.

2 S. Kim, T. Kim, W. Oh, J. Choi and S. Sun, Synergistic enhancement of microstructural homogeneity and mechanical strength in SiO_x@ C anodes via a graphene nanoribbon-based conductive agent, *J. Power Sources*, 2025, **644**, 237060.

3 N. Jin, Z. Su, Y. Niu, H. Song, X. Chen and J. Zhou, Silicon-Based Anode Materials for Lithium-Ion Batteries, *Prog. Chem.*, 2015, **27**(9), 1275–1290.

4 Y. P. Wu, E. Rahm and R. Holze, Carbon anode materials for lithium ion batteries, *J. Power Sources*, 2003, **114**(2), 228–236.

5 A. F. Martino, J. Jeon, H.-Ho Park, H. Lee and C. S. Lee, Bubble Wrap-Like Carbon-Coated Rattle-Type Silica@ silicon Nanoparticles by Surface-Protected Etching as Hybrid Anodes for Lithium–Ion Batteries, *Batteries*, 2024, **10**(2), 53.

6 C. K. Chan, H. Peng, G. Liu, K. McIlwrath, X. F. Zhang, R. A. Huggins and Y. Cui, High-performance lithium battery anodes using silicon nanowires, *Nat. Nanotechnol.*, 2008, **3**(1), 31–35.

7 Y. X. Yin, L. J. Wan and Y. G. Guo, Silicon-based nanomaterials for lithium-ion batteries, *Chin. Sci. Bull.*, 2012, **57**, 4104–4110.

8 A. N. Dey, Electrochemical alloying of lithium in organic electrolytes, *J. Electrochem. Soc.*, 1971, **118**(10), 1547–1549.

9 B. A. Boukamp, G. C. Lesh and R. A. Huggins, All-solid lithium electrodes with mixed-conductor matrix, *J. Electrochem. Soc.*, 1981, **128**(4), 725–729.

10 M. V. Reddy, G. V. Subba Rao and B. V. R. Chowdari, Metal oxides and oxysalts as anode materials for Li ion batteries, *Chem. Rev.*, 2013, **113**(7), 5364–5457.

11 T. Long and Y. Guo, Research on the temperature radius stratification model based on electrochemical-thermal-force coupling in Lithium-ion batteries, *Electrochem. Commun.*, 2025, 108052.

12 H. Zhang, T. Liu, K. Li, Y. Liu, J. Hu, Q. Zuo and L. Jiang, Enhanced robustness of lithium-ion battery equivalent circuit parameter identification via logarithmic transformation and Levenberg-Marquardt algorithm, *J. Energy Storage*, 2026, **152**, 120724.

13 S. Dai, F. Huang, J. Yan, Y. Y. Sun, C. Chen and H. D. Li, Construction of Protein-Like Helical-Entangled Structure in Lithium-Ion Silicon Anode Binders via Helical Recombination and Hofmeister Effect, *Advanced Science*, 2025, **12**(20), 2412769.

14 G. Xu, State-of-charge estimation method for lithium-ion batteries based on competitive SIR model, *Front. Energy Res.*, 2022, **10**, 984107.

15 D. Chatzogiannakis, I. Ghilescu, G. Giannadaki, M. Cabello, M. Casas-Cabanas and M. Rosa Palacin, Decoupling Silicon and Graphite Contribution in High-Silicon Content Composite Electrodes, *Batteries Supercaps*, 2025, **8**(10), e202500104.

16 H. Wenqian, F. Guo, J. Li and J. Xie, Influence of Physical Parameters on Lithium Dendrite Growth Based on Phase Field Theory, *Metals*, 2025, **16**(1), 41.

17 C. Xiao, J. Peng, Y. Jiao, Q. Shen, Y. Zhao, F. Zhao, H. Li and Q. Song, Strong and tough multilayer heterogeneous pyrocarbon based composites, *Adv. Funct. Mater.*, 2024, **34**(51), 2409881.

18 Z. Hou, J. Chen, Z. Yi, H. Lu, K. Xiong and M. Xu, Comparative study of the micro-mechanism of functional group selection at TMD-MXene interfaces: WSe_2-$Ti_3C_2T_x$ heterostructures via functional group substitution from group IV, V, VI, and VII as the prototype, *Appl. Surf. Sci.*, 2025, 165599.

19 Y. Fan, X. Liu, J. Shang, B. Liu, X. Lei, H. Zong, Z. Peng, C. Jiang and Y. Tang, Interfacial Phonon Scattering Enables Ultrastable and High-Power Sodium-Based Dual-Ion Batteries With Alloying Anodes, *Adv. Mater.*, 2026, e72848.

20 D. Jia, X. Li and J. Huang, A Hierarchical, Nanofibrous, Tin-Oxide/Silicon Composite Derived from Cellulose as a High-Performance Anode Material for Lithium-Ion Batteries, *ChemistrySelect*, 2017, **2**(20), 5667–5676.

21 S. Y. Lim, Bimodal porous structure tin oxide anode materials for lithium ion batteries, *J. Ind. Eng. Chem.*, 2019, **78**, 284–294.

22 Y. Tan, K. W. Wong and K. M. Ng, Novel silicon doped tin oxide–carbon microspheres as anode material for lithium ion batteries: The multiple effects exerted by doped Si, *Small*, 2017, **13**(48), 1702614.

23 Z. Wang, Z. Zhao, T. Li, Y. Yuan, X. Shen and J. Zhou, High-performance tin dioxide/graphdiyne composite anode materials for lithium/sodium-ion batteries, *J. Power Sources*, 2025, **638**, 236609.

24 B. Xiao, G. Wu, T. Wang, Z. Wei, Y. Sui, B. Shen, J. Qi, F. Wei, Q. Meng, Y. Ren, X. Xue, J. Zheng, J. Mao, K. Dai and Q. Yan, Tin antimony oxide @graphene as a novel anode material for lithium ion batteries, *Ceram. Int.*, 2022, **48**(2), 2118–2123.

25 M. Jiang, H. Zhang, F. Wang, Ze Zhang and Z. Yang, Synergistic integration of internal gradient-doping and external coating for superior performance in lithium-rich Mn-based cathodes, *Chem. Eng. Sci.*, 2025, **314**, 121819.

26 Y. Wang, Y. Wang, X. Tang, L. Zhang, D. Xiao, X. Zhang and Q. Zhao, Enhanced structural stability of P2-type Mn/Fe-based layered oxide by high entropy doping towards long-life sodium ion battery cathode, *Appl. Surf. Sci.*, 2025, **693**, 162799.

27 X. Wang, J. Chen, X. He, M. Lin, Z. Hou, C. Yu, H. Lu and K. Xiong, The impact of Ni and Zn doping on the stability, electrical and thermal conductivity of intermetallic compounds between Sn solder and Cu substrate, *Vacuum*, 2025, **240**, 114527.

28 Z. Zhang, Y. Wu, Z. Mo, X. Lei, X. Xie, X. Xue, H. Qin and H. Jiang, Research progress of silicon-based anode materials for lithium-ion batteries, *RSC Adv.*, 2025, **15**(14), 10731–10753.

29 Y. Weng, S. Xu, G. Huang and C. Jiang, Synthesis and performance of Li $[(Ni_{1/3}Co_{1/3}Mn_{1/3})_{1-x}Mg_x]O_2$ prepared from spent lithium ion batteries, *J. Hazard. Mater.*, 2013, **246**, 163–172.

30 M. Mohammadi and F. Sabzi, Thermodynamic Modeling of Hydrogen Solubility in [MDEA][Cl] Using Sanchez–Lacombe Equation of State, *Energy*, 1999, **24**, 709–730.

31 R. Caputo, F. Guzzetta and A. Angerhofer, Room-temperature synthesis of nickel borides via decomposition of $NaBH_4$ promoted by nickel bromide, *Inorg. Chem.*, 2010, **49**(19), 8756–8762.

32 P. Sehrawat, A. Abid, S. S. Islam, A. Mauger and M. Christian, Julien Nanostructured graphene oxide-based hybrids as anodes for lithium-ion batteries, *C*, 2020, **6**(4), 81.

33 H. Zheng, S. Fang, Z. Tong, G. Pang, L. Shen, H. Li, L. Yang and X. Zhang, Stabilized titanium nitride nanowire supported silicon core–shell nanorods as high capacity lithium-ion anodes, *J. Mater. Chem. A*, 2015, **3**(23), 12476–12481.

34 X. Zhou, Ya-X. Yin, Li-J. Wan and Yu-G. Guo, Facile synthesis of silicon nanoparticles inserted into graphene sheets as

improved anode materials for lithium-ion batteries, *Chem. Commun.*, 2012, **48**(16), 2198–2200.

35 S. Choi, T.-woo Kwon, A. Coskun and J. W. Choi, Highly elastic binders integrating polyrotaxanes for silicon microparticle anodes in lithium ion batteries, *Science*, 2017, **357**(6348), 279–283.

36 H. Ju Seo, H. Chan Jang, Y. Chan Kang and D.-W. Kim, Characteristics of Sn–Ni alloy powders directly prepared by spray pyrolysis, *J. Alloys Compd.*, 2009, **478**(1–2), 177–180.

37 Y. Xu, Y. Zhu, F. Han, L. Chao and C. Wang, 3D Si/C fiber paper electrodes fabricated using a combined electrospray/electrospinning technique for Li-ion batteries, *Adv. Energy Mater.*, 2015, **5**(1), 1400753.

38 J. Wang, M. Yi, P. Yang, D. Guo, R. Sun, F. Wu, X. Dai, Y. Gu, H. Chen and Y. Cheng, Effect of Ce incorporation into carbon layer on the performance of silicon-carbon composite as anode for LIBs, *Appl. Surf. Sci.*, 2023, **613**, 156044.

39 C. Li, Y. Chen, B. Wei, K. Ding, Y. Zhang, X. Shi and J. Zhou, A novel composite anode material of Si-SnO_2-graphene prepared in air for lithium ion batteries, *Int. J. Electrochem. Sci.*, 2017, **12**(12), 11701–11714.

40 K. Ding, Y. Zhao, M. Zhao, Li Yuan, J. Zhao, Y. Chen and Q. Wang, The influence of $SnCl_4$ doping on the electrochemical performance of spinel lithium titanate ($Li_4Ti_5O_{12}$) anode material, *Int. J. Electrochem. Sci.*, 2015, **10**(10), 7917–7928.

41 H.-lin Ren, Y. Su, S. Zhao, C.-wei Li, X.-min Wang and Bo-han Li, Construction of SiO_x-SnO_2 heterojunction and surface coating to achieve high-performance anode materials for lithium-ion batteries, *Electrochim. Acta*, 2025, **514**, 145688.

42 Mi Lu, Y. Tian, Y. Li, W. Li, X. Zheng and B. Huang, Synthesis and characterization of spherical-like tin-nickel alloy as anode for lithium ion batteries, *Int. J. Electrochem. Sci.*, 2012, **7**(1), 760–767.

43 C. Chen, Q.-H. Yang, Y. Yang, W. Lv, Y. Wen, P.-X. Hou, M. Wang and H.-M. Cheng, Self-assembled free-standing graphite oxide membrane, *Adv. Mater.*, 2009, **21**, 3007–3011.

44 Y. Sun, Q. Wu and G. Shi, Graphene based new energy materials, *Energy Environ. Sci.*, 2011, **4**(4), 1113–1132.

45 P. Yu, Y. Li, X. Zhao, L. Wu and Q. Zhang, Graphene-wrapped polyaniline nanowire arrays on nitrogen-doped carbon fabric as novel flexible hybrid electrode materials for high-performance supercapacitor, *Langmuir*, 2014, **30**(18), 5306–5313.

46 E. Starodub, N. C. Bartelt and K. F. McCarty, Oxidation of graphene on metals, *J. Phys. Chem. C*, 2010, **114**(11), 5134–5140.

47 D. Prasai, J. C. Tuberquia, R. R. Harl, G. Kane Jennings and I. Kirill, Bolotin. Graphene: corrosion-inhibiting coating, *ACS Nano*, 2012, **6**(2), 1102–1108.

48 Er Dequan, D. Eric, H. Kumar and V. B. Shenoy, Mn_3O_4–graphene hybrid as a high-capacity anode material for lithium ion batteries, *J. Am. Chem. Soc.*, 2010, **132**(40), 13978–13980.

49 Z.-S. Wu, W. Ren, L. Wen, L. Gao, J. Zhao, Z. Chen, G. Zhou, F. Li and H.-M. Cheng, Graphene anchored with Co_3O_4 nanoparticles as anode of lithium ion batteries with enhanced reversible capacity and cyclic performance, *ACS Nano*, 2010, **4**(6), 3187–3194.

50 D. Liu, C. Chen, Y. Hu, J. Wu, Z. Dong, Z.-zhong Xie, G. Wang, D. Qu, J. Li and D. Qu, Reduced graphene-oxide/highly ordered mesoporous SiO_x hybrid material as an anode material for lithium ion batteries, *Electrochim. Acta*, 2018, **273**, 26–33.

51 S. Hai, C. Yan, H. Yu, G. Xiao and D. Wang, Preparation and near-infrared absorption of nano-SnO_2/SiO_2 assemblies with doping and without doping, *J. Alloys Compd.*, 2009, **488**, 370–373.

52 M. Tokur, M. Y. Jin, B. W. Sheldon and H. Akbulut, Stress Bearing Mechanism of Reduced Graphene Oxide in Silicon-Based Composite Anodes for Lithium Ion Batteries, *ACS Appl. Mater. Interfaces*, 2020, **12**(30), 33855–33869.

53 C. Ni, C. Xia, W. Liu, W. Xu, Z. Shan, X. Lei, H. Qin and Z. Tao, Effect of graphene on the performance of silicon–carbon composite anode materials for lithium-ion batteries, *Materials*, 2024, **17**(3), 754.

54 X. Lu, P. Xu, W. Song, P. Zhou, M. Liao, G. Zeng, X. Hu, J. Li, M. Zhang, Q. Huang and Z. Su, Dual carbon boosts silicon-based anodes for excellent initial coulombic efficiency and cycling stability of lithium-ion batteries, *J. Alloys Compd.*, 2023, **938**, 168646.

55 B. D. Assresahegn and D. Bélanger, Effects of the Formulations of Silicon-Based Composite Anodes on their Mechanical, Storage, and Electrochemical Properties, *ChemSusChem*, 2017, **10**(20), 4080–4089.

56 W. Xiao, X. Yao and F. Zhang, Recycling of Oily Sludge as a Roadbed Material Utilizing Phosphogypsum-Based Cementitious Materials, *Adv. Civ. Eng.*, 2019, **2019**(1), 6280715.

57 P. Li, J. Y. Hwang and Y. K. Sun, Nano/microstructured silicon–graphite composite anode for high-energy-density Li-ion battery, *ACS Nano*, 2019, **13**(2), 2624–2633.

58 R. Banerjee, V.-H. Nguyen, T. Granzier-Nakajima, L. Pabbi, A. Lherbier, A. Ruth Binion, J.-C. Charlier, M. Terrones and E. W. Hudson, Strain modulated superlattices in graphene, *Nano Lett.*, 2020, **20**(5), 3113–3121.

59 W. Liu, J. Liu, M. Zhu, W. Wang, L. Wang, S. Xie, Li Wang, X. Yang, X. He and Y. Sun, Recycling of lignin and Si waste for advanced Si/C battery anodes, *ACS Appl. Mater. Interfaces*, 2020, **12**(51), 57055–57063.

60 W. Hu, K. He, S. Wu, T. Chen, X. Yu, Y. Liang, M. Zheng, Y. Xiao, H. Dong, Y. Liu and H. Hu, Ordered sandwich silicon quantum dot/Fe_3O_4/reduced graphene oxide architectures for high-performance lithium-ion batteries, *J. Alloys Compd.*, 2023, **943**, 168947.

61 H. Yu, Y. Zhang, L. Li, Z. Ding, Y. Chen, Q. Yuan, R. Sun, K. Li, L. Chen and J. Wu, SnO_2 nanoparticles embedded in 3D hierarchical honeycomb-like carbonaceous network for high-performance lithium ion battery, *J. Alloys Compd.*, 2021, **858**, 157716.

62 J. Pan, C. Sun, J. Liu, X. Zhao, C. Jiao, C. Wang and W. Qi, One-step synthesis method of flower-like Si@ NiO/rGO composites as high-performance anode for lithium-ion batteries, *J. Alloys Compd.*, 2023, **947**, 169506.

63 N. Zhang, K. Liu, H. Zhang, X. Wang, Y. Zhou, W. He, J. Cui and J. Sun, Constructing Biomass-Based Ultrahigh-Rate Performance SnO_y@ C/SiO_x Anode for LIBs via Disproportionation Effect, *Small*, 2023, **19**(1), 2204867.

64 Y. Ma, H. Tang, Y. Zhang, Z. Li, X. Zhang and Z. Tang, Facile synthesis of Si-C nanocomposites with yolk-shell structure as an anode for lithium-ion batteries, *J. Alloys Compd.*, 2017, **704**, 599–606.

65 Bo Ding, Z. Ahsan, X. Huang, Z. Cai, Y. Ma, G. Song, W. Yang and C. Wen, Preparation and electrochemical properties of high capacity silicon-based composites for lithium-ion batteries, *Synth. Met.*, 2020, **261**, 116324.

66 Y. Liu, R. Guo, H. Zhu and X. Wang, A novel propeller-like Si@ WO3@ C with boosted electrochemical properties as anode material for lithium-ion batteries, *Vacuum*, 2021, **184**, 109922.

67 Ke Wang, Y. Huang, Yu Meng and X. Qin, A facile route to synthesize hollow Si-Ni_3Sn_2 nanospheres@ reduced graphene oxide nanocomposites for high performance lithium-ion batteries, *J. Alloys Compd.*, 2017, **698**, 547–554.

68 X. Wang, Y. Xia, X. Zuo, S. J. Schaper, S. Yin, Q. Ji, S. Liang, Z. Yang, S. Xia, Y. Xiao, Z. Jin, P. Müller-Buschbaum and Ya-J. Cheng, Synergistic effects from super-small sized TiO_2 and SiO_x nanoparticles within TiO_2/SiO_x/carbon nanohybrid lithium-ion battery anode, *Ceram. Int.*, 2019, **45**(11), 14327–14337.

69 J. A. Spencer, A. L. Mock, A. G. Jacobs, M. Schubert, Y. Zhang and M. J. Tadjer, A review of band structure and material properties of transparent conducting and semiconducting oxides: Ga_2O_3, Al_2O_3, In_2O_3, ZnO, SnO_2, CdO, NiO, CuO, and Sc_2O_3, *Appl. Phys. Rev.*, 2022, **9**(1), 011315.

70 W.-joon Son, E. Cho, J. Lee and S. Han, Hydrogen adsorption and carrier generation in$LaAlO_3$–$SrTiO_3$ heterointerfaces: a first-principles study, *J. Phys.: Condens. Matter*, 2010, **22**(31), 315501.

71 G. Song and W. Zhang, First-principles study on the phase diagram and multiferroic properties of $(SrCoO_3)_1/(SrTiO_3)_1$ superlattices, *Sci. Rep.*, 2014, **4**(1), 4564.

72 S. F. Yuk and A. Asthagiri, A first-principles study of Pt thin films on $SrTiO_3$ (100): Support effects on CO adsorption, *J. Chem. Phys.*, 2015, **142**(12), 124704.